A surface-aware projection basis for quasigeostrophic flow

K. Shafer Smith*

Center for Atmosphere Ocean Science

Courant Institute of Mathematical Sciences

New York University

New York, NY

Jacques Vanneste

School of Mathematics

University of Edinburgh

Edinburgh, United Kingdom

Submitted to JPO

15 June 2012

Corresponding author address: K. Shafer Smith, Courant Institute of Mathematical Sciences, New York University, 251 Mercer St., New York, NY 10012.

E-mail: shafer@cims.nyu.edu

ABSTRACT

Recent studies indicate that altimetric observations of the ocean's mesoscale eddy field reflect the combined influence of surface buoyancy and interior potential vorticity anomalies. The former have a surface-trapped structure, while the latter have a more grave form. To assess the relative importance of each contribution to the signal, it is useful to project the observed field onto a set of modes that separates their influence in a natural way. However, the surface-trapped dynamics are not well-represented by standard baroclinic modes; moreover, they are dependent on horizontal scale.

Here we derive a modal decomposition that results from the simultaneous diagonalization of the energy and a generalization of potential enstrophy that includes contributions from the surface buoyancy fields. This approach yields a family of orthonomal bases that depend on two parameters: the standard baroclinic modes are recovered in a limiting case, while other choices provide modes that represent surface and interior dynamics in an efficient way.

For constant stratification, these modes consist of symmetric and antisymmetric exponential modes that capture the surface dynamics, and a series of oscillating modes that represent the interior dynamics. Motivated by the ocean, where shears are concentrated near the upper surface, we also consider the special case of a quiescent lower surface. In this case, the interior modes are independent of wavenumber, and there is a single exponential surface mode that replaces the barotropic mode. We demonstrate the use and effectiveness of these modes by projecting the energy in a set of simulations of baroclinic turbulence.

1. Introduction

Because direct observations of the ocean's interior are sparse, satellite altimetry plays a crucial role in determining its time-dependent, three-dimensional velocity structure. This indirect measurement process assumes that sea surface height variations are dominated by currents with low-mode vertical structure, a result of the stiffening action of rotation and ensuing barotropization. Observations provide some support for this assumption, at least on lateral scales of order the first internal deformation scale and above. For example, using currentmeter records in conjunction with satellite obervations, Wunsch (1997) argues that the bulk of the ocean's eddy kinetic energy resides in the barotropic and first baroclinic modes. In addition, a number of studies show a strong correlation between the lateral size of eddies and the first internal deformation scale (e.g. Stammer 1997; Chelton et al. 2011).

However, recent theoretical developments, supported by simulation and improved analysis of satellite altimetry, suggest that surface signals are not well-correlated with low-mode vertical structure, especially for submesoscale motions. In particular, Lapeyre and Klein (2006) argue that surface buoyancy and upper-ocean potential vorticity are anti-correlated for eddying flow, and that the three-dimensional velocity field may be obtained, assuming quasigeostrophy, from knowledge of the surface buoyancy field alone. The dynamics at the upper surface in this view are closely related to the surface quasigeostrophic (SQG) model (Blumen 1982; Held et al. 1995), and imply a vertical structure with a surface-trapped component that is not well represented by standard baroclinic modes. This view is supported by results from simulations (LaCasce and Mahadevan 2006; Klein et al. 2008), as well as recent analyses of satellite altimetry (e.g. Isern-Fontanet et al. 2006; Le Traon et al. 2008). Finally, in an atmospheric context, Tulloch and Smith (2009) have shown that lateral surface buoyancy gradients may interact with interior mean potential vorticity gradients to excite baroclinically unstable modes that generate SQG-like dynamics near the upper surface. In simulations, the resulting kinetic energy spectrum near the surface exhibits a steep -3 slope just below the deformation scale, and a flatter $-5/3$ slope at smaller scales — translated to

the oceanic context, this implies an energetic submesoscale dominated by the surface mode.

One of the most widely used tools in oceanography is the projection of the vertical structure of observed or simulated currents on simple bases of functions. The above observations and modeling results lead one to seek projection bases that faithfully represent both the low-mode interior structure and the surface dynamics. The standard basis of baroclinic modes, consisting of the eigenfunctions $\phi(z)$ of the operator $\partial_z[f^2/N^2(z)\ \partial_z\phi]$, with homogenous boundary conditions $\partial_z\phi|_{z=0} = \partial_z\phi|_{z=-H} = 0$, fails in this respect. By construction, it is a complete basis in which to expand the streamfunction ψ of flows provided they satisfy the same homogeneous boundary conditions, which imply zero surface and bottom buoyancy. But for realistic flows with non-zero surface buoyancy $b = f\partial_z\psi|_{z=0}$, expansion in baroclinic modes leads to a non-uniform convergence near $z = 0$, and a very large set of modes is required to capture the near-surface behaviour.

As noted by Lapeyre and Klein (2006), in quasigeostrophic theory, the dynamical contribution of the surface buoyancy can be separated from that of the interior potential vorticity: taking advantage of the linearity of the inversion of the quasigeostrophic potential vorticity (PV)

$$q = \nabla^2\psi + \partial_z\left(\frac{f^2}{N^2}\ \partial_z\psi\right) \tag{1}$$

the streamfunction may be decomposed into interior and surface parts, $\psi = \psi^{\mathrm{int}} + \psi^{\mathrm{surf}}$ (assuming zero buoyancy at the bottom), where ψ^{int} satisfies (1) with boundary condition $\partial_z\psi^{\mathrm{int}}|_{z=0} = 0$ while ψ^{surf} satisfies the zero-PV condition $\nabla^2\psi^{\mathrm{surf}} + \partial_z(f^2/N^2\ \partial_z\psi^{\mathrm{surf}}) = 0$ with $\partial_z\psi^{\mathrm{surf}}|_{z=0} = b/f$. The vertical structure of the interior contribution can be expanded in the standard baroclinic modes. By contrast, the surface contribution — the only one retained in SQG theory — has a vertical structure determined by the zero PV condition which couples horizontal and vertical dependence, reducing to $\exp(\kappa Nz/f)$, where κ is the horizontal wavenumber, in the case of constant N and for $z \gg H$.

It is intuitively clear that an effective projection basis should somehow combine modes similar to the baroclinic modes with modes that, like the exponential modes of SQG theory,

2

capture the dynamical contribution of the surface buoyancy. A systematic method to obtain such a basis has remained elusive, however. Tulloch and Smith (2009) proposed a heuristic model based on a barotropic and first baroclinic mode, appended by exponential modes for each surface. Similarly, Lapeyre (2009) attempted to represent the full dynamics of the upper ocean with a truncated set of standard baroclinic modes appended by an exponential surface mode. However, these hybrid modes do not diagonalize the energy, since the surface and interior modes are not orthogonal. Moreover, because the surface modes depend on wavenumber while the interior modes do not, the energetic overlap varies with horizontal scale, increasing with increasing scale. These difficulties stem from the fact that the addition of the exponential mode makes the basis functions linearly dependent in a certain sense, leading to an overcomplete frame rather than a basis. A consequence is that the modal decomposition is non-unique. Lapeyre (2009) defined a unique basis by requiring that it minimizes a certain functional, but the results remained inconclusive. An alternative basis, involving modes satisfying the Dirichlet condition $\psi|_{z=0} = 0$ together with the barotropic mode, has recently been proposed by Scott and Furnival (2012) but this too suffers from a lack of orthogonality.

In this paper, we take a different approach and propose a new modal basis (or rather a family of bases) that diagonalizes the energy and effectively captures surface-intensified motion driven by buoyancy. Our approach relies on the observation that there are infinitely many possible (complete) bases onto which the flow may be projected which diagonalize the energy. As we show, a useful basis is obtained by demanding that it simultaneously diagonalizes both the energy and another quadratic invariant that generalizes potential enstrophy to include the variances of the surface and bottom buoyancy fields. The relative weight of the potential enstrophy and buoyancy variances in this invariant provide two parameters that determine the basis uniquely.

The eigenvalue problem that arises is similar to the standard vertical mode problem, but retains a dependence on horizontal wavenumber, and the eigenvalue appears in both the

3

eigenvalue equation and its boundary conditions. In a limiting case, the standard baroclinic modes are recovered — for constant N and $-H \leq z \leq 0$, these are $\psi_n \propto \cos(n\pi z/H)$, $n = 0, 1, \ldots$. Another limiting case, motivated by the ocean where shears are concentrated near the upper surface but are weak at depth, leads to the simple basis

$$\psi_0 \propto \cosh\left[N\kappa(z+H)/f\right], \quad \psi_n \propto \sin\left[(n-1/2)\pi z/H)\right], \, n = 1, 2, \ldots \tag{2}$$

which includes the exponential mode of SQG theory.

The paper is organized as follows. In section 2 we construct a generalized eigenvalue problem that defines the new basis. In section 3, we derive analytical solutions and general results for two special cases: constant N, for expository purposes, and an ocean-like case, in which the lower boundary is assumed quiescent, leading to (2). These modes are tested in section 4 on fields generated from a set of high-resolution quasigeostrophic simulations of baroclinic turbulence. Finally, we discuss and conclude in section 5.

2. Surface-aware basis

Throughout the paper, we assume a horizontally-periodic domain bounded vertically by rigid surfaces at $z = z^-$ and $z = z^+$, with total depth $H = z^+ - z^-$. The horizontal periodicity allows us to Fourier transform the equations in the horizontal plane, resulting in separable dynamics and ordinary differential equations for the vertical structure. (In more general domains, the Fourier series can be replaced by an expansion in eigenfunctions of the horizontal Laplacian, and the results obtained here should hold essentially unchanged.) The complex amplitudes of the quasigeostrophic potential vorticity (PV) $q = q_{kl}(z)$, surface buoyancies (SBs) $b_{kl}^{\pm}$ and streamfunction $\psi = \psi_{kl}(z)$ are then related by

$$\left(\frac{f^2}{N^2}\psi'\right)' - \kappa^2\psi = q, \quad z^- < z < z^+ \tag{3a}$$

$$\frac{f^2}{N^2 H}\psi' = b^{\pm}, \quad z = z^{\pm}, \tag{3b}$$

4

where $\kappa = (k^2 + l^2)^{1/2}$ is the wavenumber magnitude, a prime indicates a z derivative, f is the Coriolis frequency and $N = N(z)$ is the buoyancy frequency. We include the non-standard factor $f^2/(N^2 H)$ in our the definition of the SBs so that the SBs and PV have the same dimension (inverse time), and because it ultimately yields a more natural eigenvalue problem. We have omitted the wavenumber subscript on q, $b^\pm$ and ψ and continue to do so onward, except where confusion may occur.

The quasigeostrophic equation set has four quadratic invariants: energy, potential enstrophy, and the buoyancy variance at each surface. At each wavenumber κ, these are

$$E_\kappa = \frac{1}{2H} \int_{z^-}^{z^+} \left(\frac{f^2}{N^2} |\psi'|^2 + \kappa^2 |\psi|^2 \right) \, \mathrm{d}z$$

$$Z_\kappa = \frac{1}{2H} \int_{z^-}^{z^+} |q|^2 \, \mathrm{d}z$$

$$B_\kappa^\pm = \frac{1}{2} |b^\pm|^2.$$

Summing each quantity over (k, l) gives the total invariant.

We seek to define a complete basis that diagonalizes the energy. This can be done in infinitely many ways. Our strategy is based on the following principles: (i) we regard the energy as a functional, not of the streamfunction, but of the PV and of the SBs; (ii) we exploit standard results on the simultaneous diagonalization of quadratic forms. Principle (i) is grounded in the quasigeostrophic model, which makes it explicit that PV and SBs, taken together, make up the set of dynamical variables. Thus, the contribution of the SBs to the dynamics is recognized; as a result, the bases we obtain naturally represent data with non-zero surface buoyancies. Regarding (ii), we recall a classical result from linear algebra: whereas there are infinitely many bases diagonalizing a quadratic form $\boldsymbol{x}^\mathrm{T} \mathsf{A} \boldsymbol{x}$, where A is a symmetric positive definite matrix, only one of these bases also diagonalizes another quadratic form $\boldsymbol{x}^\mathrm{T} \mathsf{B} \boldsymbol{x}$ (e.g. Horn and Johnson 1990). This is simply found by solving the generalized eigenvalue problem $\mathsf{B} \boldsymbol{x} = \lambda \mathsf{A} \boldsymbol{x}$. An analogous result applies to linear operators (see, e.g. Goldstein 1980). Similarly, here we can define a unique basis by insisting that it diagonalizes another quadratic form in addition to the energy E_κ. A natural choice for this

is a 'generalized potential enstrophy' that combines the remaining invariants into a single quantity,

$$P_\kappa \equiv Z_\kappa + \alpha_+ B^+ + \alpha_- B^- \tag{4}$$

where $\alpha_\pm > 0$ are (nondimensional) undetermined weights, the choice of which will be discussed later. This approach yields a unique basis for fixed $\alpha_\pm$.

To proceed, we require four objects: a vector structure that combines the SBs and interior PV, an inner product that operates on this vector, and two operators (analogous to the matrices A and B above) that give the energy and generalized potential enstrophy in terms of the inner product. These are defined as follows:

Vector. We define the 'generalized potential vorticity vector'[1]

$$\boldsymbol{Q} \equiv \begin{pmatrix} b^+ \\ q(z) \\ b^- \end{pmatrix}. \tag{5}$$

Inner product. The specific choice of inner product is unimportant for the final results; we make what appears to be the simplest choice, namely

$$\langle \boldsymbol{Q}_1, \boldsymbol{Q}_2 \rangle = \frac{1}{H} \int_{z^-}^{z^+} \bar{q}_1 q_2 \ \mathrm{d}z + \bar{b}_1^+ b_2^+ + \bar{b}_1^- b_2^- , \tag{6}$$

where the overbar denotes a complex conjugate.

Operators. With the definitions (5) and (6), it is a simple matter to find the linear operators $\mathcal{E}$ and $\mathcal{P}$ such that

$$E_\kappa = \frac{1}{2} \langle \boldsymbol{Q}, \mathcal{E}\boldsymbol{Q} \rangle \quad \text{and} \quad P_\kappa = \frac{1}{2} \langle \boldsymbol{Q}, \mathcal{P}\boldsymbol{Q} \rangle. \tag{7}$$

---

[1]Notice that our $\boldsymbol{Q}$ bears a resemblance to the generalized potential vorticity of Bretherton (1966), which in our notation is written

$$Q_{\mathrm{B}} = \left(\frac{f^2}{N^2} \psi' \right)' - \kappa^2 \psi - \frac{f^2}{N^2} \psi' \delta(z - z^+) + \frac{f^2}{N^2} \psi' \delta(z - z^-).$$

Our notation makes it plain that the PV and SBs are independent, a point that the use of Q_{B} might obscure.

6

These are given by

$$
\mathcal{E}\boldsymbol{Q} = \begin{pmatrix} \psi(z^+) \\ -\psi(z) \\ -\psi(z^-) \end{pmatrix} \quad \text{and} \quad \mathcal{P}\boldsymbol{Q} = \begin{pmatrix} \alpha_+ b^+ \\ q(z) \\ \alpha_- b^- \end{pmatrix},
\tag{8}
$$

where the streamfunction ψ is the solution of (3), given q and $b^\pm$. The first of these expressions is obtained after an integration by parts; the second is immediate. These two operators are positive definite and self-adjoint (see Appendix 5 for details).

The basis we seek is now given by the eigenfunctions $\boldsymbol{\xi}_n$ of the generalized eigenvalue problem

$$
\mathcal{P}\boldsymbol{\xi}_n = \mu_n^2 \mathcal{E}\boldsymbol{\xi}_n,
\tag{9}
$$

where the eigenvalues μ_n^2 are positive for all n. To obtain an explicit form for (9), we define the components of $\boldsymbol{\xi}_n = [\xi_n^+, \xi_n(z), \xi_n^-]^{\mathrm{T}}$ analogous to those of $\boldsymbol{Q}$, and the scalar streamfunctions $\phi_n(z)$ such that $\mathcal{E}\boldsymbol{\xi}_n = [\phi_n(z^+), -\phi_n(z), -\phi_n(z^-)]^{\mathrm{T}}$. In terms of these, the eigenvalue problem reads

$$
\begin{pmatrix} \alpha_+\xi_n^+ \\ \xi_n(z) \\ \alpha_-\xi_n^- \end{pmatrix} = \mu_n^2 \begin{pmatrix} \phi_n(z^+) \\ -\phi_n(z) \\ -\phi_n(z^-) \end{pmatrix}.
\tag{10}
$$

In view of (3), this implies that the ϕ_n satisfy

$$
\left(\frac{f^2}{N^2}\phi_n' \right)' - \kappa^2\phi_n = -\mu_n^2\phi_n \quad \text{and} \quad \frac{f^2}{N^2 H}\phi_n' = \pm\frac{\mu_n^2}{\alpha_\pm}\phi_n \quad \text{at} \quad z = z^\pm.
\tag{11}
$$

This eigenvalue problem is a key result of the paper. Its eigenfunctions ϕ_n, which are purely real, give the form of the streamfunction corresponding to the basis eigenvectors $\boldsymbol{\xi}_n$. The three components of these eigenvectors may be derived from the ϕ_n using (10), although, as shown below, this is not necessary to project data onto the modes $\boldsymbol{\xi}_n$.

By construction, the eigenfunctions are orthogonal for the products $\langle \cdot, \mathcal{E}\cdot \rangle$ and $\langle \cdot, \mathcal{P}\cdot \rangle$. The choice of normalization for the eigenvectors $\boldsymbol{\xi}_n$ is inessential, but it is convenient to fix

7

the energy of each mode to be unity, that is, to take

$$\langle \boldsymbol{\xi}_m, \mathcal{E}\boldsymbol{\xi}_n \rangle = \frac{1}{H} \int_{z^-}^{z^+} \left(\frac{f^2}{N^2} \phi'_m \phi'_n + \kappa^2 \phi_m \phi_n \right) \, \mathrm{d}z = \delta_{mn}. \tag{12}$$

The expression in terms of ϕ_m and ϕ_n is found by using (10) and (11) to eliminate $\boldsymbol{\xi}_m$, $\boldsymbol{\xi}_n$ and the eigenvalues, then integrating by parts, which removes boundary terms. Correspondingly,

$$\langle \boldsymbol{\xi}_m, \mathcal{P}\boldsymbol{\xi}_n \rangle = \frac{\mu_n^2}{H} \int_{z^-}^{z^+} \left(\frac{f^2}{N^2} \phi'_m \phi'_n + \kappa^2 \phi_m \phi_n \right) \, \mathrm{d}z = \mu_n^2 \delta_{mn} \tag{13}$$

and

$$\langle \mathcal{P}^{-1}\mathcal{E}\boldsymbol{\xi}_m, \mathcal{E}\boldsymbol{\xi}_n \rangle = \frac{1}{H} \int_{z^-}^{z^+} \phi_m \phi_n \, \mathrm{d}z + \frac{\phi_m(z^+)\phi_n(z^+)}{\alpha_+} + \frac{\phi_m(z^-)\phi_n(z^-)}{\alpha_-} = \mu_n^{-2} \delta_{mn}. \tag{14}$$

The latter relation (14) has the advantage of involving only the undifferentiated streamfunctions, while the first relation (12) is independent of the eigenvalues and $\alpha_{\pm}$.

The basis of eigenfunctions can be used to expand data: given $\boldsymbol{Q}$ or ψ, we can write

$$\boldsymbol{Q} = \sum_n a_n \boldsymbol{\xi}_n \quad \text{and} \quad \psi = \sum_n a_n \phi_n, \tag{15}$$

where the a_n are amplitude coefficients that can be found using one of the orthogonality relations (12) or (13); for instance

$$a_n = \langle \boldsymbol{\xi}_n, \mathcal{E}\boldsymbol{Q} \rangle = \frac{1}{H} \int_{z_-}^{z_+} \left(\frac{f^2}{N^2} \phi'_n \psi' + \kappa^2 \phi_n \psi \right) \, \mathrm{d}z.$$

The energy and generalized potential enstrophy are then simply

$$E_\kappa = \frac{1}{2} \sum_n |a_n|^2 \quad \text{and} \quad P_\kappa = \frac{1}{2} \sum_n \mu_n^2 |a_n|^2, \tag{16}$$

respectively.

Note that, even though the eigenvalue problem (11) is not of the standard Sturm–Liouville form, because of the presence of the eigenvalue μ_n^2 in the boundary conditions, the basis of eigenvectors can be shown to be complete in the sense that it provides a representation of arbitrary vectors $\boldsymbol{Q}$ that converges as the number of modes tends to ∞. This is discussed further in Appendix 5.

8

194   Lastly, note that our choice of orthogonality conditions implies slightly unfamiliar dimen-

195 sions for the eigenfunctions. Because $[q], [b^\pm] \sim [T^{-1}]$ and $[\mu] \sim [L^{-1}]$ (where T is time, L is

196 length, and braces mean "dimensions of"), (9) implies that $[\boldsymbol{\xi}] \sim [L^{-2}][\phi]$. The orthogonality

197 condition (12) demands $[\phi] \sim [L]$ and therefore $[\boldsymbol{\xi}] \sim [L^{-1}]$. In the next section, the problem

198 will be analyzed in an appropriate nondimensional form.

3. Structure of the surface-aware modes and special cases

201   The approach described above provides a family of bases parameterized by the values

202 of α_+ and α_-. In principle, different values can be chosen for different wavenumbers κ;

203 here, however, we restrict attention to choices of $\alpha_\pm$ that are independent of κ. To clarify

204 some general properties of the new modes, we first recast the eigenvalue problem in non-

205 dimensional form with the substitutions $z \mapsto Hz$, $\kappa \mapsto f/(N_0 H)\,\kappa$ and $\mu \mapsto f/(N_0 H)\,\mu$,

206 where N_0 is a typical value of N; thus the wavenumber and eigenvalue are scaled by the

207 approximate deformation length, $N_0 H/f$. The non-dimensional eigenvalue problem (11)

208 then becomes

$$(s\phi_n')' = -\lambda_n^2 \phi_n \quad \text{and} \quad s\phi_n' = \pm\frac{\lambda_n^2 + \kappa^2}{\alpha_\pm}\phi_n \ \text{ at } \ z = 0, -1, \quad \text{where} \quad s = \frac{N_0^2}{N^2(z)} \quad (17)$$

209 and we have defined an alternative eigenvalue λ_n such that

$$\mu_n^2 = \kappa^2 + \lambda_n^2. \tag{18}$$

210 Written in terms of λ_n, the eigenvalue equation takes the form of the standard vertical mode

211 equation, but with more complicated boundary conditions.

212   Analysis of the new eigenvalue problem (17) is complicated by its dependence on three

213 independent parameters: κ, α_+ and α_-. Moreover, for each choice of parameters, there is

214 an infinite set of eigenvalues. Since the problem depends on the two weights $\alpha_\pm$ in a nearly

equivalent way, we proceed first by setting the weights equal and defining $\alpha \equiv \alpha_+ = \alpha_-$ (a case in which the weights differ will be considered in a later subsection). The nature of the eigenproblem is then largely determined by the size of the boundary condition coefficient μ_n^2/α: when $\mu_n^2/\alpha \to 0$, the boundary conditions revert to the standard case $\phi_n' = 0$ at the top and bottom, while when $\mu_n^2/\alpha \to \infty$, the boundary conditions become $\phi_n = 0$ at the top and bottom. However, more subtle possibilities arise as well, because unlike the standard vertical mode problem, λ_n may be imaginary (although μ_n is always real). When λ_n is real, the modes are oscillatory, but when it is imaginary, the modes are evanescent — these can be interpreted either as surface modes or as extensions of the barotropic mode.

This interpretation is suggested by examining the eigenvalue problem in two limiting regimes:

$\kappa^2 \ll \alpha$: modes with real λ satisfy the simplified boundary condition $(s\phi_n') = \pm\lambda_n^2\phi_n/\alpha$ at $z = 0, -1$ which further reduces to $\phi_n' = 0$ for $\alpha \gg 1$, corresponding to the standard baroclinic modes.[2] These are complemented by a barotropic mode for which the first approximation $\lambda = 0$ can be refined to the purely imaginary $\lambda = i\kappa\sqrt{2/\alpha}$.

$\kappa^2 \gg \alpha$. In this case, almost all modes have $\mu_n^2 = \kappa^2 + \lambda_n^2 \gg \alpha$ and hence satisfy the simplified boundary conditions $\phi_n = 0$ at $z = 0, -1$. There are two additional modes, however, for which $\mu_n^2 = O(\alpha)$ and hence $\lambda \sim i\kappa$. These solve

$$(s\phi_n')' - \kappa^2\phi_n \simeq 0 \quad \text{with} \quad s\phi_n' = \pm\frac{\mu_n^2}{\alpha_\pm}\phi_n \ \text{ at } \ z = 0, -1, \tag{19}$$

and can be recognized as surface modes, with zero interior PV.

---

[2]This approximation is not uniform in n but breaks down for highly oscillatory modes, with $\lambda_n = O(\alpha)$, which satisfy $\phi' = O(\alpha) \neq 0$ at $z = 0, -1$ and thus differ from the standard high-n baroclinic modes.

a. Analytical solutions for constant N

In the special case of constant stratification, or $s = 1$, the eigenvalue problem (17) can be solved in closed form. Writing the solutions as

$$\phi_n = A\cos(\lambda_n z) + B\sin(\lambda_n z),$$

where A and B are integration constants, and imposing the boundary conditions leads to an algebraic equation for λ_n, which may be either real or imaginary. For $\lambda_n^2 > 0$, the characteristic equation (dropping the subscript n) is

$$\tan\lambda = \frac{(\alpha_+ + \alpha_-)\lambda(\lambda^2 + \kappa^2)}{(\lambda^2 + \kappa^2)^2 - \alpha_+\alpha_-\lambda^2}. \tag{20}$$

For $\lambda^2 < 0$ we define $\tilde{\lambda} = i\lambda$ and obtain

$$\tanh\tilde{\lambda} = \frac{(\alpha_+ + \alpha_-)\tilde{\lambda}(\kappa^2 - \tilde{\lambda}^2)}{(\kappa^2 - \tilde{\lambda}^2)^2 + \alpha_+\alpha_-\tilde{\lambda}^2}. \tag{21}$$

Equations (20) and (21) are suitable for a graphical analysis. Fig. 1 shows that there are infinitely many solutions to (20) (top panel) and one or two solutions to (21) depending on $\alpha_\pm$ (bottom panel; in both cases we set $\alpha \equiv \alpha_+ = \alpha_-$). An important parameter is the ratio of the slopes of the right- and left-hand sides of (20) and (21) at $\lambda = 0$, which in both cases is

$$\frac{\alpha_+ + \alpha_-}{\kappa^2} \equiv \tilde{\kappa}^{-2}$$

When $\tilde{\kappa} < 1$ there is only one solution to (21), and there is a solution of (20) with $\lambda < \pi/2$. On the other hand, if $\tilde{\kappa} > 1$, there are two solutions to (21) (note that the maximum of the right-hand side of (21) is 1), and there may or may not be a solution of (20) for $\lambda < \pi/2$.[3]

The solution to (21) gives either a generalization of the barotropic mode, in the case of a single solution, or two modes that capture the vertical structure of the surface modes. Setting

---

[3]Note also that if $\alpha_+\alpha_- > 4\kappa^2$, the denominator of the right-hand side of (20) goes to 0, but stays finite otherwise: the existence of a 0 in the denominator determines whether there is a solution to (20) with $\lambda < \pi/2$ in the case $\tilde{\kappa}^{-2} > 1$.

11

251 $\alpha \equiv \alpha_+ = \alpha_-$, these solutions are plotted as functions of $\tilde{\kappa}$ in Fig. 2: there are two solutions

252 when $\tilde{\kappa} > 1$, but only one otherwise. The limiting solutions discussed in the previous section

253 can be derived explicitly. In the limit $\tilde{\kappa}^2 = \kappa^2/(2\alpha) \ll 1$, the single solution of (21) is given

254 by $\tilde{\lambda} \sim \kappa\sqrt{2/\alpha}$, with eigenfunction $\phi \propto 1$, which can be interpreted as the barotropic mode.

255 For $\tilde{\kappa}^2 \gg 1$, the two solutions can be identified as surface intensified modes, one symmetric

256 and the other antisymmetric about the center of the domain, explicitly given by

$$\phi_0 \propto \cosh\left[\kappa(z + \tfrac{1}{2})\right] \quad \text{and} \quad \phi_1 \propto \sinh\left[\kappa(z + \tfrac{1}{2})\right],$$

257 with eigenvalues $\mu_0/\alpha = \kappa\tanh\kappa$ and $\mu_1/\alpha = \kappa\coth\kappa$. For $\kappa \gg 1$, the eigenvalues are nearly

258 identical, so that linear combinations of the eigenfunctions will also satisfy the eigenvalue

259 problem — in particular, one can construct separate upper-surface and lower-surface modes.

260 For real λ, the right-hand side of (20) tends to zero for both large and small κ, leading to

261 eigenvalues $\lambda_n = n\pi$, $n = 1, 2\ldots$ The eigenfunctions, however, differ in the two cases: for

262 $\tilde{\kappa} \ll 1$, they have the standard form $\phi_n \propto \cos(n\pi z)$, but for $\tilde{\kappa} \gg 1$, they are $\phi_n \propto \sin(n\pi z)$.

263 The first four modes, for $\alpha = 1$ and a range of κ are plotted in Fig. 3.

264 *b. An oceanic special case*

Here we consider a case that is potentially the most relevant to the ocean, where shears

near the surface may lead to surface-intensified modes, while the quiescent abyss may be

more naturally represented by the standard boundary condition, $\phi' = 0$ at the bottom. The

relevant limits for this case are $\alpha_+ \ll 1$ and $\alpha_- \to \infty$, in which case the eigenvalue problem

reduces to

$$(s\phi_n')' = -\lambda_n^2\phi_n, \quad \text{with} \quad \phi_n|_{z=0} = 0, \qquad \phi_n'|_{z=-1} = 0, \qquad (22a)$$

$$(s\phi_0')' - \kappa^2\phi_0 = 0, \qquad \text{with} \quad s\phi_0'|_{z=0} = \frac{\mu_0^2}{\alpha_+}\phi_0, \quad \phi_0'|_{z=-1} = 0. \qquad (22b)$$

265 to leading order in α_+. The solutions ϕ_n, $n = 1, 2\ldots$ to (22a) describe interior modes, while

266 ϕ_0 is the solution to (22b) with $\mu_0^2/\alpha_+ = O(1)$ and represents a zero PV, surface-intensified

267 mode.

12

268   Note that the structure of the interior modes, like that of the standard baroclinic modes, is
269 independent of κ; the normalization of the mode energy that we have chosen however leads to
270 κ-dependent normalization factors. Since we concentrate on the leading-order approximation
271 to the eigenvalue problem as $\alpha_+ \to 0$, all the modes, including the surface-intensified one, are
272 independent of α_+ and so are the normalisation factors (because the energy does not involve
273 α_+). Only the eigenvalue μ_0^2 depends (linearly) on α_+, although the approximation $\mu_0^2 = 0$
274 can be made to conclude, in particular, that the surface-intensified mode has a generalized
275 enstrophy which vanishes to leading order.

276   Recently, Scott and Furnival (2012) proposed to use the eigenfunctions of (22a), forming
277 what they term a Dirichet basis, in conjunction with the barotropic mode. While this set
278 of functions, like that obtained by adding a surface mode to the standard baroclinic basis
279 (Lapeyre 2009), does not diagonalize the energy, it is remarkable that this is achieved by
280 the complete set of solutions of (22a) and (22b), that is, by the Dirichlet basis plus a surface
281 mode.

    For constant N (or $s = 1$), the solutions to (22) may be computed explicitly; they are

$$\phi_0 = A \cosh\left[\kappa(z+1)\right], \qquad A \equiv \sqrt{\frac{2}{\kappa \sinh(2\kappa)}} \tag{23a}$$

$$\phi_n = B \sin\left[\left(n - \frac{1}{2}\right)\pi z\right], \qquad B \equiv \sqrt{\frac{2}{\pi^2(n-1/2)^2 + \kappa^2}} \tag{23b}$$

282 with eigenvalues $\mu_0^2 = \alpha_+ \kappa \tanh\kappa$ (corresponding to $\tilde{\lambda} \simeq \kappa - (\alpha_+/2)\tanh\kappa$) and $\lambda_n =$
283 $(n-1/2)\pi$ with $n = 1, 2 \ldots$. Their dimensional form was given by (2) in the introduction.
284 Again, note that the dependence on κ of the coefficient for the interior modes is due to the
285 normalization choice, but is irrelevant for the projection of data.

4.   Use of new basis for the projection of simulated data

287   As a demonstration, we use the new basis to project the energy in three simulated tur-
288 bulent flows, each generated by baroclinic instability of a fixed mean state in a horizontally-

₂₈₉ periodic quasigeostrophic model. The numerical model is spectral in the horizontal, and

₂₉₀ finite-difference in the vertical — it is the same as used in, for example, Smith and Ferrari

₂₉₁ (2009). Energy is dissipated by linear bottom drag, and enstrophy is removed by a highly

₂₉₂ scale-selective exponential cutoff filter (Smith et al. 2002). In all cases, the model resolution

₂₉₃ is $512 \times 512 \times 100$.

₂₉₄   We analyze results from three simulations. These first two are based on highly idealized

₂₉₅ flows, and will be used to demonstrate the fundamental structure of the basis, and how

₂₉₆ the partition of energy depends on both the nature of the flow, and on the choice of the

₂₉₇ nondimensional weights $\alpha_{\pm}$. The third simulation is based on a more realistic, ocean-like

₂₉₈ mean state, and is designed to explore the oceanic special case considered at the end of

₂₉₉ the last section. To project the simulated data onto the new basis, one must consider the

₃₀₀ generalized matrix eigenvalue problem that results from the particular vertical discretization

₃₀₁ used in the model. The details of the construction of the basis in this discretization are given

₃₀₂ explicitly Appendix B.

₃₀₃ *a. Idealized 'interior' and 'surface' baroclinic instability simulations*

₃₀₄   Both idealized flows have constant stratification $s = 1$, a ratio of domain scale to defor-

₃₀₅ mation scale equal to 4 and $\beta = 0$, but mean states that generate different types of baroclinic

₃₀₆ instability. The first simulation, is forced by an 'interior instability,' with a mean flow that

₃₀₇ projects onto the first (standard) baroclinic mode, $U(z) = \cos \pi z$. Flows of this type are

₃₀₈ unstable due to a sign change of the mean interior PV gradient, but have no mean SB gra-

₃₀₉ dients, since $B_y^{\pm} \propto U_z|_{z=0,-1} = 0$ — we refer to this simulation as BC1. The second flow

₃₁₀ is forced by an Eady mean state, with a linear mean shear $U(z) = z$, so the instability is

₃₁₁ driven by mean SB gradients $B_y^{\pm} = 1$, resulting in energy generation near the two surfaces.

₃₁₂   The simulations are run to statistically steady state, and snapshots of the steady-state

₃₁₃ prognostic fields of each are used to compute horizontal (total) energy spectra. The upper

₃₁₄ panels of Fig. 4, display the horizontal spectra for the BC1 (left) and Eady (middle) simu-

14

lations for a few vertical levels z (the right-hand column plots will be discussed in the next subsection). It is immediately apparent that the energy in the BC1 simulation is spread rather evenly over depth; by contrast, the energy in the Eady simultion is largly concentrated at the two surfaces. The panels in the middle row of Fig. 4 show the first few modes of the energy projected onto the standard basis, $\phi_n(z) \propto \cos(n\pi z)$, $n = 1, 2, ...$ (the baroclinic modes) and $\phi_0 \propto 1$ (the barotropic mode). Consistent with the z-dependence of the energy in the upper panel, the energy in BC1 is largely captured by the barotropic and first baroclinic modes. By contrast, the energy in the Eady case seems to be distributed evenly across the barotropic and a large number of baroclinic modes, effectively demonstrating the failure of the standard modes to provide any insight into the energy partition in a case with large energy near the surfaces.

The bottom panels of Fig. 4 display the energy spectra for the first few modes in the projection onto the new basis (BC1, left panel; Eady, middle panel). Anticipating that the BC1 simulation is best represented by the standard baroclinic basis (recovered from the generalized basis in the limit $\alpha_\pm \gg 1$), while the Eady simulation is best represented on the generalized basis in the limit $\alpha_\pm \ll 1$, we chose $\alpha_\pm = 10^6$ for the former and $\alpha_\pm = 10^{-4}$ for the latter. As is apparent, the generalized basis with the appropriate weights more efficiently captures the surface energy in the Eady simulation much better than the standard basis.

To quantify the choice of $\alpha_\pm$, we consider the projection of energy in both the BC1 and Eady simulations with the generalized basis using weights ranging from $\alpha_\pm = 10^{-3}$ to 10^3 (always holding $\alpha = \alpha_+ = \alpha_-$) and ask, for what weights is the energy captured by the least number of modes? A simple diagnostic for this, the ratio of the energy contained in the first two modes to the total energy as a function of α, is shown in in Fig. 5. The results indicate that extreme values of α are best suited for the BC1 ($\alpha \to \infty$) and Eady ($\alpha \to 0$) simulations, thus confirming our choice for Fig. 4. In the next section we examine a third simulation where the interior and surface contributions are more balanced, so that intermediate values of $\alpha_\pm$ may be expected to be relevant.

b. A semi-realistic oceanic simulation

The third simulation is driven by a mean state typical of the mid-latitude ocean. It uses an exponential mean stratification $N^2 = N_0^2 \exp(z/h)$, so that $s = \exp(-z/h)$, with $h = 0.2$, intended to represent the pycnocline. The mean shear is $U(z) = h(z+1-h)\exp(z/h)+g(z)+C$, where $g(z)$ is the first standard baroclinic eigenfunction of the operator $(sg')' = -\lambda^2 g$, with $g' = 0$ at $z = 0, -1$, so that U is surface-intensified with $U'(0) = 1$ and $U'(-1) = 0$. The constant C is set to ensure $\int_{-1}^{0} U(z)\,dz = 0$. Both $U(z)$ and $N(z)$ are plotted in the top panel of Fig. 6. Note that U is baroclinically unstable due to both an internal sign change of the mean PV gradient, and to the interaction of the mean interior PV gradient Q_y with the mean upper SB gradient B_y^+. Consistent with the assumptions of the ocean modes, the lower SB gradient $B_y^- = 0$. The ratio of the domain scale to the first baroclinic deformation radius (as determined by λ^{-1}) is 5. The nondimensional Coriolis gradient $\beta U_0 L_D^{-2} = 1.2$, and energy is dissipated by a linear drag $r L_d U_0^{-1} = 0.4$. The steady-state turbulent flow has a complicated vertical structure, as evidenced by the vertical slice of the PV shown in Fig. 7.

The energy spectra for the flow are shown in the right panels of Fig. 4, just as for the BC1 and Eady cases. The energy spectra by vertical level again indicates a very surface-intensified flow, but this time, the flow falls off from a $-5/3$ spectral slope to a more energetic interior than was the case for the Eady simulation. Projection onto the standard vertical modes (middle right panel) indicates a peak in the barotropic mode, but otherwise energy is spread evenly over a large number of baroclinic modes. Projection onto a generalized basis is shown in the bottom right panel. For this simulation with no buoyancy activity at the bottom, it is natural to use a basis with $\alpha_- \to \infty$. The maximum in the ratio of the energy in modes 1 and 2 to total energy shown in Fig. 5 suggests that the value $\alpha = \alpha_+ = 2$ is appropriate. The first few modes of the corresponding basis are shown in the bottom panels of Fig 6. This is the basis chosen for Fig. 4, and indicates that the projection is very effective, with most of the energy captured by the surface and modified first baroclinic modes. An alternative basis is the 'oceanic' basis of section b which takes $\alpha_+ \ll 1$. The spectra obtained with this

16

369 basis (not shown) are essentially identical to those obtained for $\alpha_+ = 2$. This suggests that

370 the results are insensitive to the precise value of α_+ and that 'oceanic' basis may be a good

371 default choice to analyse typical ocean data.

5. Conclusion

373 This paper presents a family of basis functions designed for the projection of three-

374 dimensional ocean velocity data. The bases diagonalize both the quasigeostrophic energy and

375 a generalization of the quasigeostrophic potential enstrophy that includes contributions from

376 the buoyancy variances at the upper and lower surfaces. The family of bases is parameterized

377 by the weights $\alpha_\pm$ assigned to the surface buoyancy variances — the standard baroclinic

378 modes are recovered in the limit $\alpha_\pm \to \infty$, but the modes obtained in the opposite limit

379 allow for efficient representation of the surface buoyancy variances. The bases should prove

380 advantageous in a number of applications, from projection of observations to the derivation

381 of highly truncated theoretical models. Their main drawback compared to the standard basis

382 of baroclinic modes is the dependence of the modes on the wavenumber κ which implies a lack

383 of separation between the horizontal vertical structure in physical space. This drawback is

384 unavoidable if some of the modes are to reflect the SQG contribution; it is minimised for the

385 'oceanic' basis obtained for $\alpha_+ \to 0$, $\alpha_- \to \infty$ since all but one modes have a κ-independent

386 structure.

387 The limit $\alpha_- \to \infty$ would seem a natural choice of generalized basis for typical ocean

388 conditions takes because of the relative lack of buoyancy activity at the bottom. Regarding

389 α_+, an optimal value can in principle be chosen by inspecting the spectra for a range of

390 values or by using a diagnostic such as that of Fig. 5. However, some simpler rules of thumb

391 would be desirable. Intuitively, one might expect that the optimal values of $\alpha_\pm$ are those

392 that balance the contributions of the enstrophy Z_κ and of the surface-buoyancy variance B_κ^+

393 in the generalized enstrophy $P_\kappa = Z_\kappa + \alpha_+ B_\kappa^+$. Some support for this intuition is provided

17

by Fig. 8 which shows Z_κ, B_κ and their ratio as a function of κ for the ocean simulation. The figure shows a ratio Z_κ/B_κ^+ that is around 5 for a broad range of κ, roughly consistent with the value $\alpha_+ = 2$ indicated by Fig. 5. There is, however, a peak around $\kappa = 4$ and a substantial increase for $\kappa \gtrsim 20$, which suggest that better results could be obtained by allowing α_+ to depend on κ. We have not explored this intriguing possibility here.

As an alternative to the ratio $Z_\kappa/B_\kappa^\pm$, it would be useful to relate more directly the value of the weights $\alpha_\pm$ most appropriate to project a flow on the large-scale characteristics of the flow. Since for flows driven by instabilities, Z_κ and $B_\kappa^\pm$ are related to the large-scale PV and surface-buoyancy gradients Q_y and $B_y^\pm$, it is plausible that the ratio $Q_y/B_y^\pm$ can be used as a guide for the choice of the weights.

The advent of higher-resolution satellite observations, expected when the Surface Water Ocean Topography satellite becomes operational (Fu and Ferrari 2008), will improve our understanding of upper-ocean submesoscale dynamics only to the extent that we can connect surface observations with the three-dimensional structure of the flow below the surface. The basis derived and demonstrated here may prove a useful tool in this goal.

APPENDIX A

Derivation details

Here we prove a few relevant facts about the eigenvectors and eigenvalues of (9). First, we show that the operator $\mathcal{E}$ is self-adjoint, e.g. $\langle \boldsymbol{\xi}_m, \mathcal{E}\boldsymbol{\xi}_n \rangle = \langle \mathcal{E}\boldsymbol{\xi}_m, \boldsymbol{\xi}_n \rangle$. Expanding the left-hand side and integrating by parts, we find

$$
\begin{aligned}
\langle \boldsymbol{\xi}_m, \mathcal{E}\boldsymbol{\xi}_n \rangle &= \frac{1}{H} \int_{z^-}^{z^+} -\bar{\xi}_m \phi_n \, \mathrm{d}z + \bar{\xi}_m^+ \phi_n(z^+) - \bar{\xi}_m^- \phi_n(z^-), \\
&= \frac{1}{H} \int_{z^-}^{z^+} -\phi_n \left(\frac{f^2}{N^2} \bar{\phi}'_m \right)' + \kappa^2 \bar{\phi}_m \phi_n \, \mathrm{d}z \\
&\quad + \frac{f^2}{HN^2(z^+)} \bar{\phi}'_m(z^+) \phi_n(z^+) - \frac{f^2}{HN^2(z^-)} \bar{\phi}'_m(z^-) \phi_n(z^-), \\
&= \frac{1}{H} \int_{z^-}^{z^+} \frac{f^2}{N^2} \phi'_n \bar{\phi}'_m + \kappa^2 \bar{\phi}_m \phi_n \, \mathrm{d}z, \\
&= \langle \mathcal{E}\boldsymbol{\xi}_m, \boldsymbol{\xi}_n \rangle
\end{aligned}
$$

since the expression on the penultimate line is clearly symmetric. The self-adjointness of $\mathcal{P}$

as well as the positive definiteness is obvious.

To establish the completeness of the basis of the eigenvector $\boldsymbol{\xi}_n$, we rewrite the eigenvalue

problem in the standard form $\mathcal{A}\boldsymbol{\xi}_n = \mu_n^{-2} \boldsymbol{\xi}_n$, where $\mathcal{A} = \mathcal{P}^{-1}\mathcal{E}$ is positive definite and self-

adjoint. This operator is compact when acting on the Hilbert space of vectors $\boldsymbol{Q}$ with

bounded norm $\langle \boldsymbol{Q}, \boldsymbol{Q} \rangle$. This is because it is essentially an integral operator with continuous

kernel — the Green's function of the operator $(s\phi')' - \kappa^2 \phi$ (e.g. Debnath and Mikusiński

1998, section 4.8). The Hilbert-Schmidt theorem (Debnath and Mikusiński 1998, section

4.10) then applies to guarantee that every vector $\boldsymbol{Q}$ has a unique convergent expansion in

terms of the $\boldsymbol{\xi}_n$.

APPENDIX B

Discrete eigenvalue problem and numerical computation

of modes

Here we construct the discrete version of the eigenvalue problem. Assuming a constant discrete coordinate z_j on J grid points, with $z_1 = 0$ at the top, $z_J = -H$ at the bottom, and a constant finite difference $\Delta z = z_j - z_{j+1}$, the mean stratification is $N_0^2 = (g/\rho_0)\overline{\Delta\rho}/\Delta z$, where $\overline{\Delta\rho} = \rho_J - \rho_1$ is the average background density jump between levels, $\rho_j = \rho(z_j)$ is the background density, and ρ_0 is the average density. The parameter $s = N_0^2/N^2$ is discretized as $s_j = s(z_{j+1/2}) \equiv \overline{\Delta\rho}/(\rho_{j+1} - \rho_j)$, thus s_j is offset by a half space from ρ_j. In this discretization, the SBs and PV are

$$b^+ = \frac{f^2}{N_0^2 H}\,s\psi'|_{z=0} \;\longrightarrow\; L_D^{-2}\,\frac{s_1}{\delta}(\psi_1 - \psi_2)$$

$$b^- = \frac{f^2}{N_0^2 H}\,s\psi'|_{z=-1} \;\longrightarrow\; L_D^{-2}\,\frac{s_{J-1}}{\delta}(\psi_{J-1} - \psi_J)$$

$$q = \left(\frac{f^2}{N_0^2}s\psi'\right)' - \kappa^2\psi \;\longrightarrow\; L_D^{-2}\,\frac{1}{\delta^2}\left[s_{j-1}\psi_{j-1} - (s_{j-1} + s_j)\psi_j + s_j\psi_{j+1}\right] - \kappa^2\psi_j,$$

where $\delta \equiv \Delta z/H$ and $L_D \equiv N_0 H/f$. Nondimensionalizing $\kappa \mapsto [L_D^{-1}]\,\kappa$, $\psi \mapsto [L_D^2 T^{-1}]\,\psi$
and $(q, b^\pm) \mapsto [T^{-1}]\,(q, b^\pm)$ (for some timescale T), the discrete PV/SBs and streamfunction
are related as

$$\boldsymbol{Q} = \mathsf{A}\boldsymbol{\psi},$$

where

$$
\mathsf{A} = \frac{1}{\delta^2}
\begin{pmatrix}
\delta s_1 & -\delta s_1 & 0 & \dots\dots\dots\dots\dots\dots\dots\dots\dots\dots & 0 \\
s_1 & -(s_1 + s_2 + \delta^2\kappa^2) & s_2 & 0 & \dots\dots\dots\dots\dots\dots\dots\dots\dots & 0 \\
& & & \dots\dots\dots\dots & & \\
0 & \dots\dots\dots\dots\dots\dots & 0 & s_{J-2} & -(s_{J-2} + s_{J-1} + \delta^2\kappa^2) & s_{J-1} \\
0 & \dots\dots\dots\dots\dots\dots\dots & 0 & & \delta s_{J-1} & -\delta s_{J-1}
\end{pmatrix}.
\tag{B1}
$$

Defining the operators

$$
\mathsf{B} =
\begin{pmatrix}
1 & 0 & \dots & 0 \\
0 & \delta & \dots & 0 \\
& & & \\
0 & \dots & \delta & 0 \\
0 & \dots & 0 & 1
\end{pmatrix}
\quad \text{and} \quad
\mathsf{F} =
\begin{pmatrix}
1 & 0 & \dots & 0 \\
0 & -1 & \dots & 0 \\
& & & \\
0 & \dots & 0 & -1
\end{pmatrix},
\tag{B2}
$$

one sees that B plays the part of the inner product, e.g. $\langle \boldsymbol{\xi}_1, \boldsymbol{\xi}_2 \rangle \to \boldsymbol{\xi}_1^T \mathsf{B} \boldsymbol{\xi}_2$ and F accomplishes the awkard sign changes in the definition of the operator $\mathcal{E}$. The energy in wavenumber κ is

$$
E_\kappa = \frac{\delta}{2} \left[\sum_{j=1}^{J-1} s_j \left| \frac{\psi_j - \psi_{j-1}}{\delta} \right|^2 + \kappa^2 \sum_{j=2}^{J-1} |\psi_j|^2 \right] = \frac{1}{2} \boldsymbol{\psi}^* \mathsf{FBA} \boldsymbol{\psi}.
$$

For consistency with the theoretical development in section 2, we may also write the energy in terms of the vector $\boldsymbol{Q} = \mathsf{A}\boldsymbol{\psi}$,

$$
E_\kappa = \frac{1}{2} \boldsymbol{Q}^* \mathsf{BFA}^{-1} \boldsymbol{Q} = \frac{1}{2} \boldsymbol{Q}^* \mathsf{B}\mathcal{E} \boldsymbol{Q}
$$

where the symmetry of F and B were used, and $\mathcal{E} \equiv \mathsf{FA}^{-1}$ is defined to make the discrete version of the energy operator defined in (8) perfectly clear.

Similarly, the generalized enstrophy in wavenumber κ is

$$
P_\kappa = \frac{1}{2} \boldsymbol{Q}^* \mathsf{B}\mathcal{P} \boldsymbol{Q}
$$

22

where we define

$$\mathcal{P} = \begin{pmatrix} \alpha_+ & 0 & \dots & 0 \\ 0 & 1 & \dots & 0 \\ & & & \\ 0 & \dots & 1 & 0 \\ 0 & \dots & 0 & \alpha_- \end{pmatrix}$$

to make clear the analogy with the generalized enstrophy operator defined in (8).

Now note that $\mathsf{B}\mathcal{E}$ and $\mathsf{B}\mathcal{P}$ are both symmetric (the former can be verified by checking that FBA is symmetric), so we can simultaneously diagonalize the two quadratic forms E_κ and P_κ by solving the generalized eigenvalue problem $\mathsf{B}\mathcal{P}\boldsymbol{\xi}_j = \mu_j^2 \mathsf{B}\mathcal{E}\boldsymbol{\xi}_j$ or, in matrix form

$$(\mathsf{B}\mathcal{P})\mathsf{X} = (\mathsf{B}\mathcal{E})\mathsf{X}\mathsf{M}^2$$

where X is the matrix with columns $\boldsymbol{\xi}_j$ and M^2 has μ_j^2 along is its diagonal and zeros elsewhere. Solutions to this generalized eigenvalue problem obey the orthogonality relations

$$\mathsf{X}^\top \mathsf{B}\mathcal{E}\mathsf{X} = \mathsf{I} \quad \text{and} \quad \mathsf{X}^\top \mathsf{B}\mathcal{P}\mathsf{X} = \mathsf{M}^2, \tag{B3}$$

which are analogous to (12) and (13), respectively.

In practice, it is more convenient to define a streamfunction eigenfunction $\boldsymbol{\phi}$ such that $\mathsf{A}\boldsymbol{\phi} = \boldsymbol{\xi}$, so that the generalized eigenvalue problem can be rewritten as $\mathsf{F}\mathcal{P}\mathsf{A}\boldsymbol{\phi}_j = \mu_j^2 \boldsymbol{\phi}_j$, or in matrix form

$$\mathsf{F}\mathcal{P}\mathsf{A}\Phi = \Phi\mathsf{M}^2 \tag{B4}$$

where Φ has $\boldsymbol{\phi}_j$ as its columns. In this case, the orthogonality relations become

$$\Phi^\top \mathsf{FBA}\Phi = \mathsf{I} \quad \text{and} \quad \Phi^\top \mathcal{P}\mathsf{BA}^2\Phi = \mathsf{M}^2, \tag{B5}$$

where we've used the fact that $\mathsf{F}^2 = \mathsf{I}$. Finally, writing (B4) as $\Phi^{-1}(\mathsf{A}^{-1}\mathcal{P}^{-1}\mathsf{F})\Phi = \mathsf{M}^2$ and using the first relation in (B5), we have the equivalent of (14),

$$\Phi^{-1}\mathsf{B}\mathcal{P}^{-1}\Phi = \mathsf{M}^{-2} \tag{B6}$$

23

The expansion in the basis of eigenvectors $\boldsymbol{\phi}_n$ of discrete data is readily expressed in terms of the matrix $\boldsymbol{\Phi}$. Denoting by $\boldsymbol{\psi}$ the column vector of the streamfunction data (Fourier transformed in the horizontal) $\psi(z_j)$, the expansion reads

$$\boldsymbol{\psi} = \boldsymbol{\Phi}\mathbf{a}, \tag{B7}$$

where $\mathbf{a} = (a_1, \ldots, a_J)^\top$ is the column vector of the mode amplitudes. These amplitudes are obtained from the data using the relation

$$\mathbf{a} = \boldsymbol{\Phi}^\top \mathsf{F}\mathsf{B}\mathsf{A}\boldsymbol{\psi},$$

which is deduced from (B5) and (B7). The total energy at a given wavenumber κ,

$$E_\kappa = \frac{1}{2}\boldsymbol{\psi}^* \mathsf{F}\mathsf{B}\mathsf{A}\boldsymbol{\psi} = \frac{1}{2}|\mathbf{a}|^2,$$

where $*$ denotes the complex (conjugate) transpose, is clearly the sum of the individual contributions $|a_n|^2/2$ of each mode. Similarly, the generalized enstrophy,

$$P_\kappa = \frac{1}{2}\boldsymbol{Q}^* \mathsf{B}\mathcal{P}\boldsymbol{Q} = \frac{1}{2}\boldsymbol{\psi}^* \mathcal{P}\mathsf{B}\mathsf{A}^2\boldsymbol{\psi} = \frac{1}{2}\mathbf{a}^*\mathsf{M}^2\mathbf{a},$$

is the sum of the contributions $\mu_n^2|a_n|^2/2$.

24

REFERENCES

Blumen, W., 1982: Wave-interactions in quasi-geostrophic uniform potential vorticity flow. *J. Atmos. Sci.*, **39 (11)**, 2388–2396.

Bretherton, F. P., 1966: Critical layer instability in baroclinic flows. *Quart. J. Roy. Meteor. Soc.*, **92**, 325–334.

Chelton, D. B., M. G. Schlax, and R. M. Samelson, 2011: Global observations of nonlinear mesoscale eddies. *Prog. in Oceanogr.*, **91**, 167–216.

Debnath, L. and P. Mikusiǹski, 1998: *Introduction to Hilbert spaces.* 2d ed., Academic Press, 551 pp.

Fu, L.-L. and R. Ferrari, 2008: Observing oceanic submesoscale processes from space. *EOS*, **89**, 488.

Goldstein, H., 1980: *Classical Mechanics.* 2d ed., Addison-Wesley.

Held, I. M., R. T. Pierrehumbert, S. T. Garner, and K. L. Swanson, 1995: Surface quasi-geostrophic dynamics. *J. Fluid. Mech.*, **282**, 1–20.

Horn, R. A. and C. R. Johnson, 1990: *Matrix Analysis.* Cambridge University Press.

Isern-Fontanet, J., B. Chapron, G. Lapeyre, and P. Klein, 2006: Potential use of microwave sea surface temperatures for the estimation of ocean currents. *Geophysical Research Letters*, **33 (24)**, doi:ARTNL24608.

Klein, P., B. L. Hua, G. Lapeyre, X. Capet, S. L. Gentil, and H. Sasaki, 2008: Upper ocean turbulence from high resolution 3d simulations. *J. Phys. Oceanogr.*, **38**, 1748–1763.

25

LaCasce, J. H. and A. Mahadevan, 2006: Estimating subsurface horizontal and vertical velocities from sea surface temperature. *J. Marine Res.*, **64**, 695–721.

Lapeyre, G., 2009: What mesoscale signal does the altimeter reflect? on the decomposition in baroclinic modes and a surface-trapped mode. *J. Phys. Oceanogr.*, **39**, 2857–2874.

Lapeyre, G. and P. Klein, 2006: Dynamics of the upper oceanic layers in terms of surface quasigeostrophy theory. *J. Phys. Oceanogr.*, **36**, 165–176.

Le Traon, P. Y., P. Klein, and B. L. Hua, 2008: Do altimeter wavenumber spectra agree with the interior or surface quasigeostrophic theory? *J. Phys. Oceanogr.*, **38**, 1137–1142.

Scott, R. B. and D. G. Furnival, 2012: Assessment of traditional and new eigenfunction bases applied to extrapolation of surface geostrophic current time series to below the surface in an idealized primitive equation simulation. *J. Phys. Oceanogr.*, **42**, 165–178.

Smith, K. S., G. Boccaletti, C. C. Henning, I. N. Marinov, C. Y. Tam, I. M. Held, and G. K. Vallis, 2002: Turbulent diffusion in the geostrophic inverse cascade. *J. Fluid Mech.*, **469**, 13–48.

Smith, K. S. and R. Ferrari, 2009: The production and dissipation of compensated thermohaline variance by mesoscale stirring. *J. Phys. Oceanogr.*, **39**, 2477–2501.

Stammer, D., 1997: Global characteristics of ocean variability estimated from regional TOPEX/Poseidon altimeter measurements. *J. Phys. Oceanogr.*, **27**, 1743–1769.

Tulloch, R. T. and K. S. Smith, 2009: Quasigeostrophic turbulence with explicit surface dynamics: Application to the atmospheric energy spectrum. *J. Atmos. Sci.*, **66**, 450–467.

Wunsch, C., 1997: The vertical partition of oceanic horizontal kinetic energy. *J. Phys. Oceanogr.*, **27**, 1770–1794.
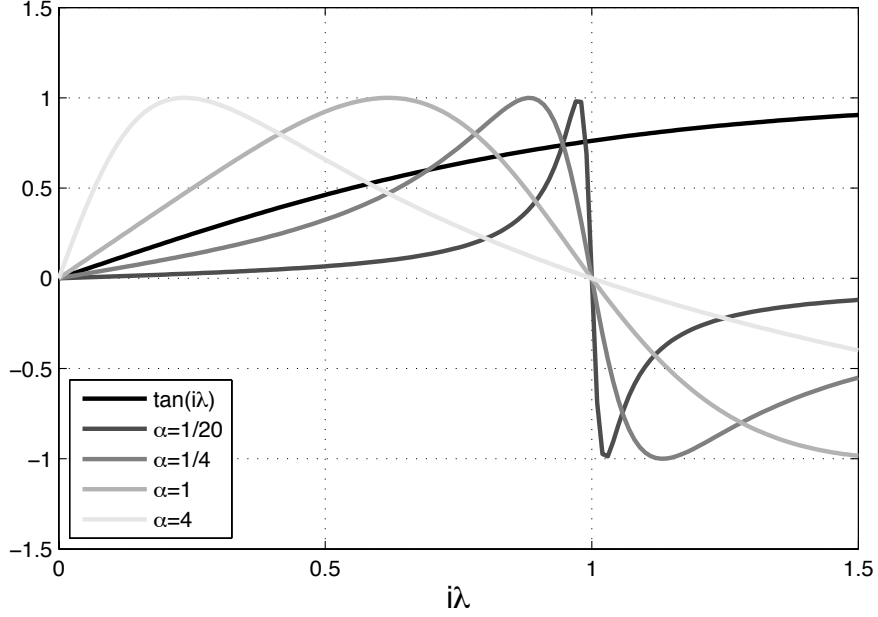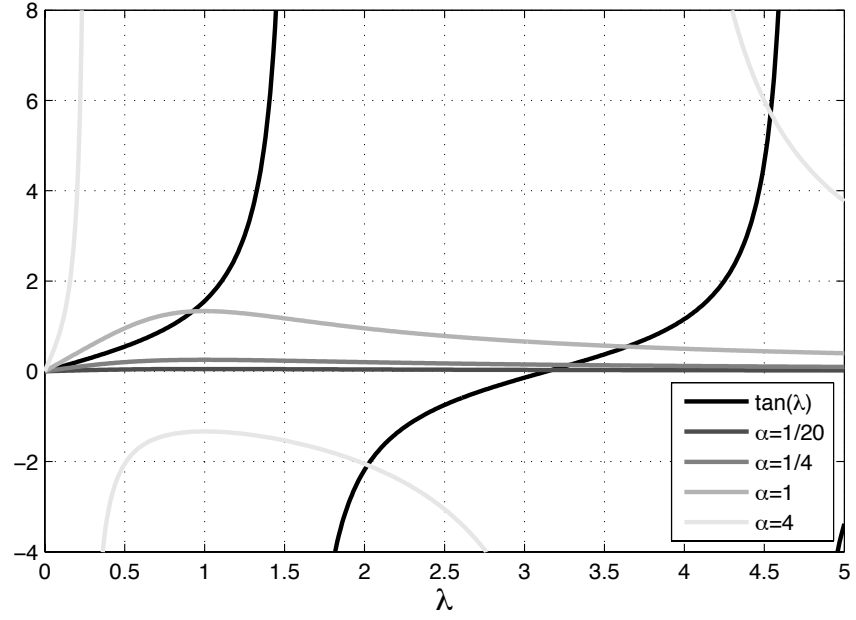
List of Figures

FIG. 1. Graphical solutions for eigenvalues with constant N for $\kappa = 1$. The left panel shows the left and right hand sides of Eq. (20), and the right panel shows Eq. (21).
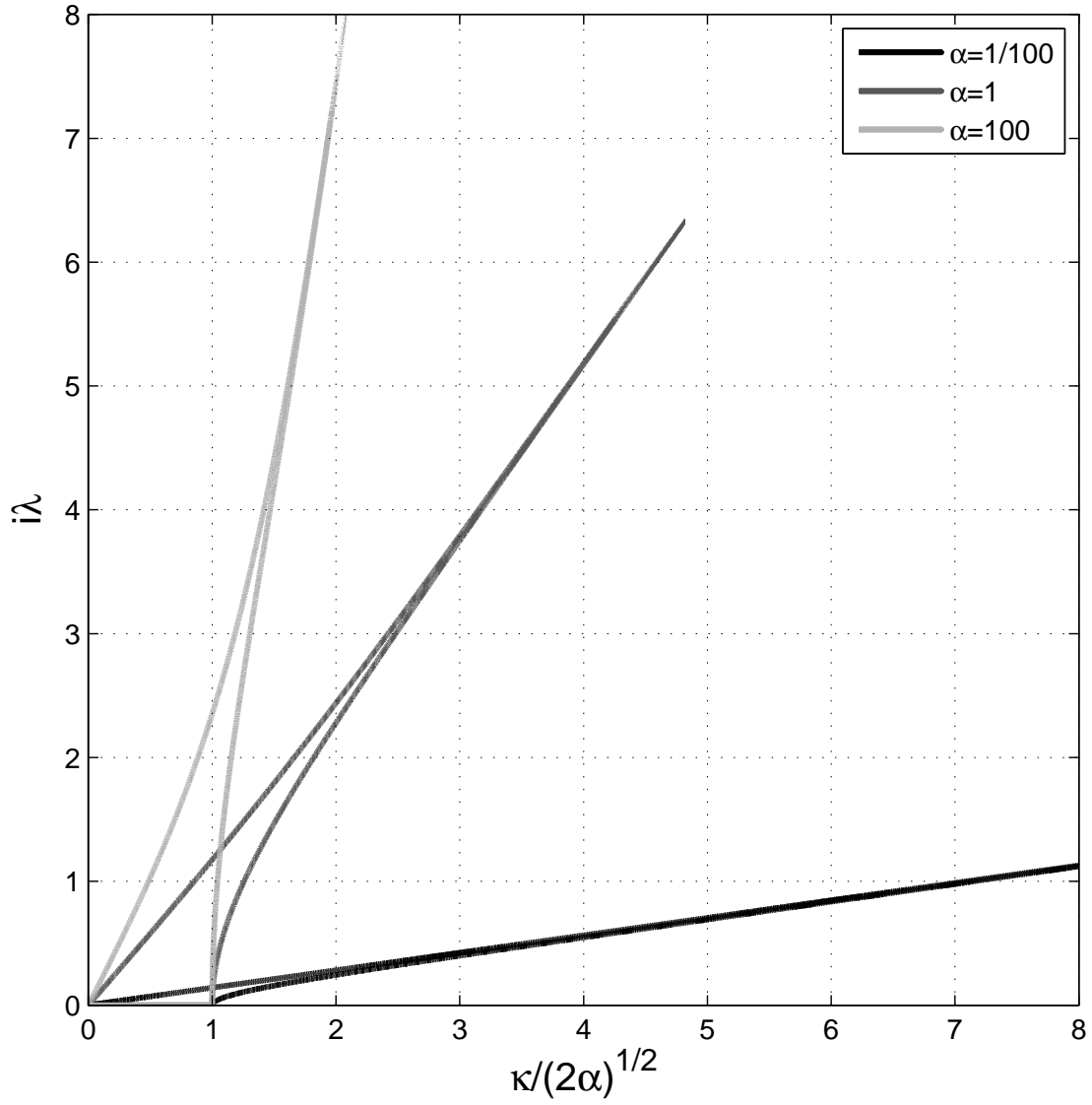
Fig. 2. Solutions to (21), with κ scaled by $\sqrt{2\alpha}$, the cutoff separating cases with one or two solutions for imaginary λ.
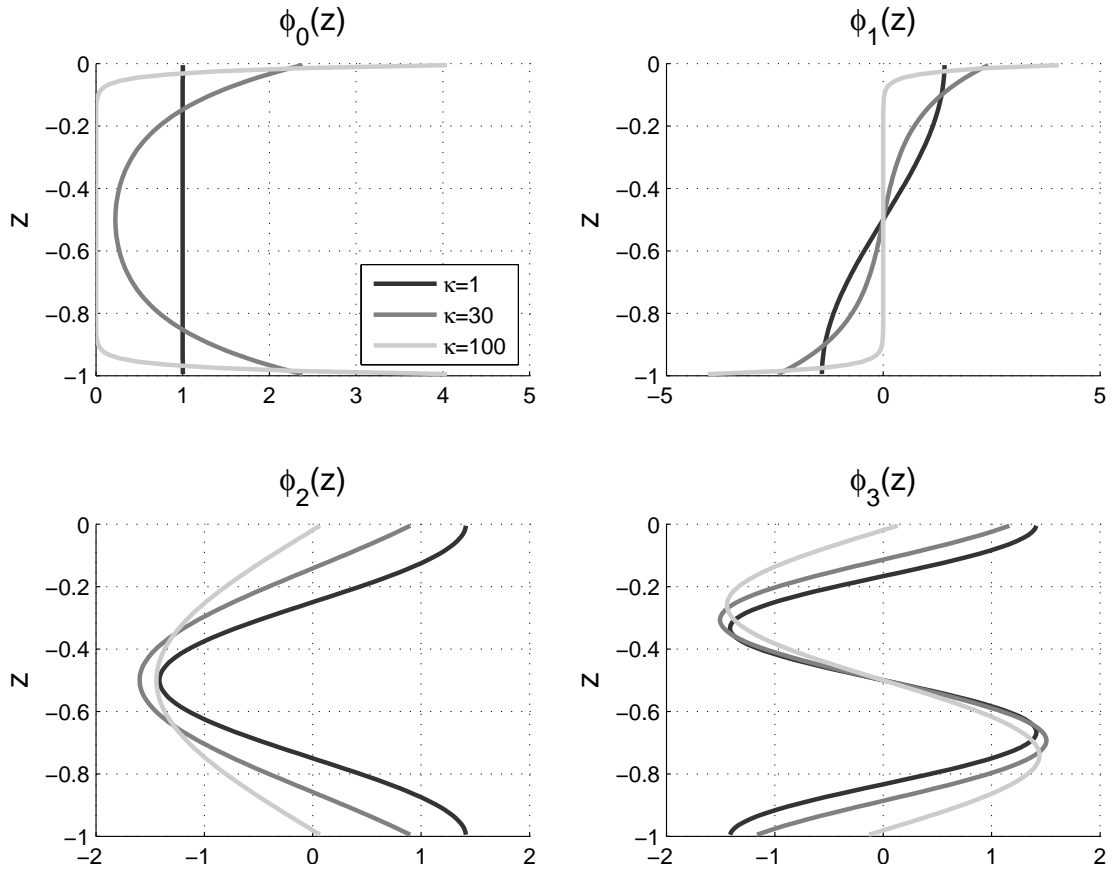
30

FIG. 3. The first four eigenfunctions ϕ_n for the constant-N case, with $\alpha_+ = \alpha_- = 100$ and $\kappa = 1, 30, 100$.
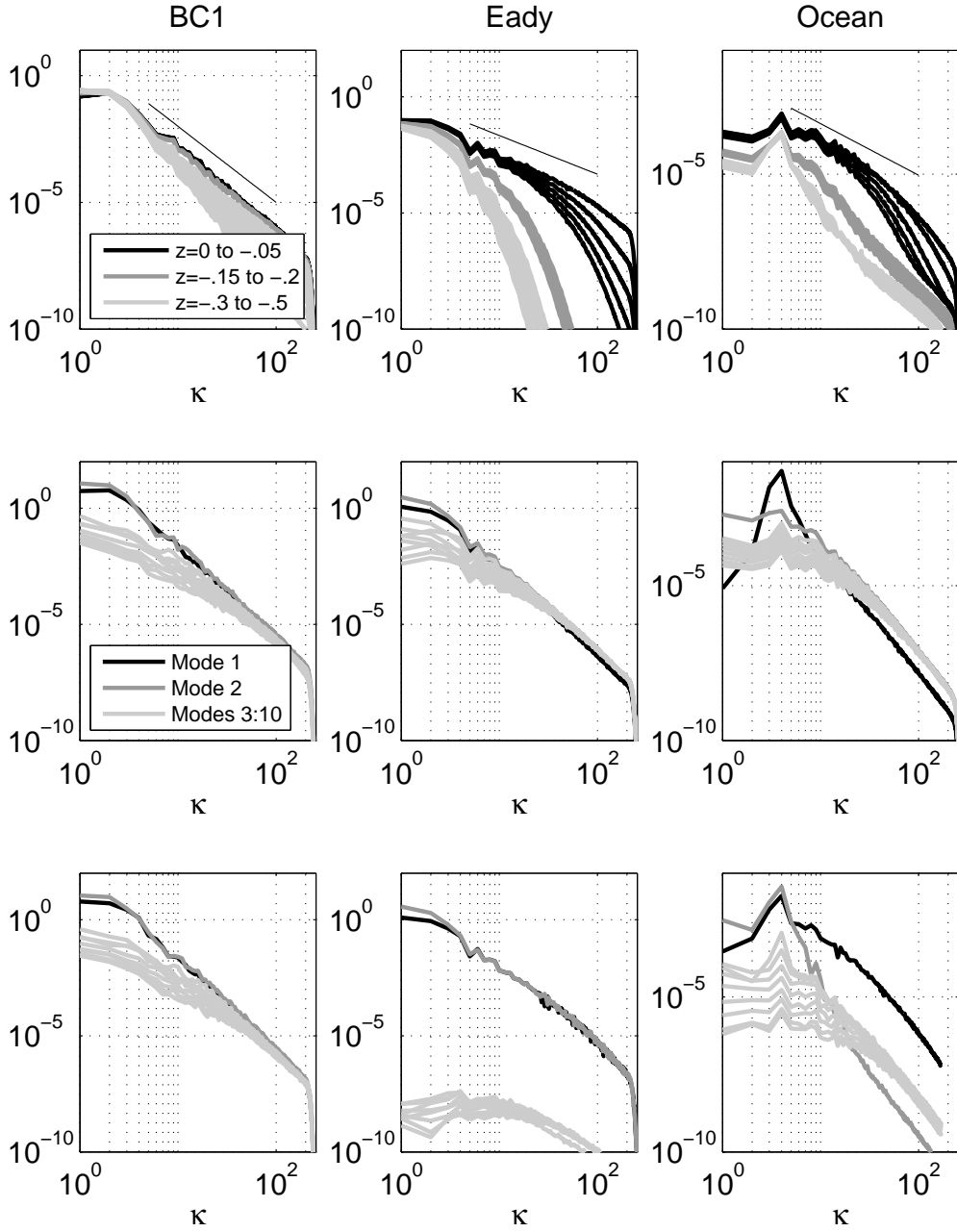
31

FIG. 4. Energy spectra for the BC1 (left), Eady (middle) and Ocean (right) simulations. Top panels: spectra for selected vertical levels (see legend). Middle: spectra from fields projected onto standard vertical modes (modes 1, 2 and 3–10 are shown). Bottom: spectra from fields projected onto new modes, with $\alpha_+ = \alpha_- = 10^6$ for the BC1 case, $\alpha_+ = \alpha_- = 10^{-4}$ for the Eady case and $\alpha_+ = 2$, $\alpha_- = 10^6$ for the Ocean case.
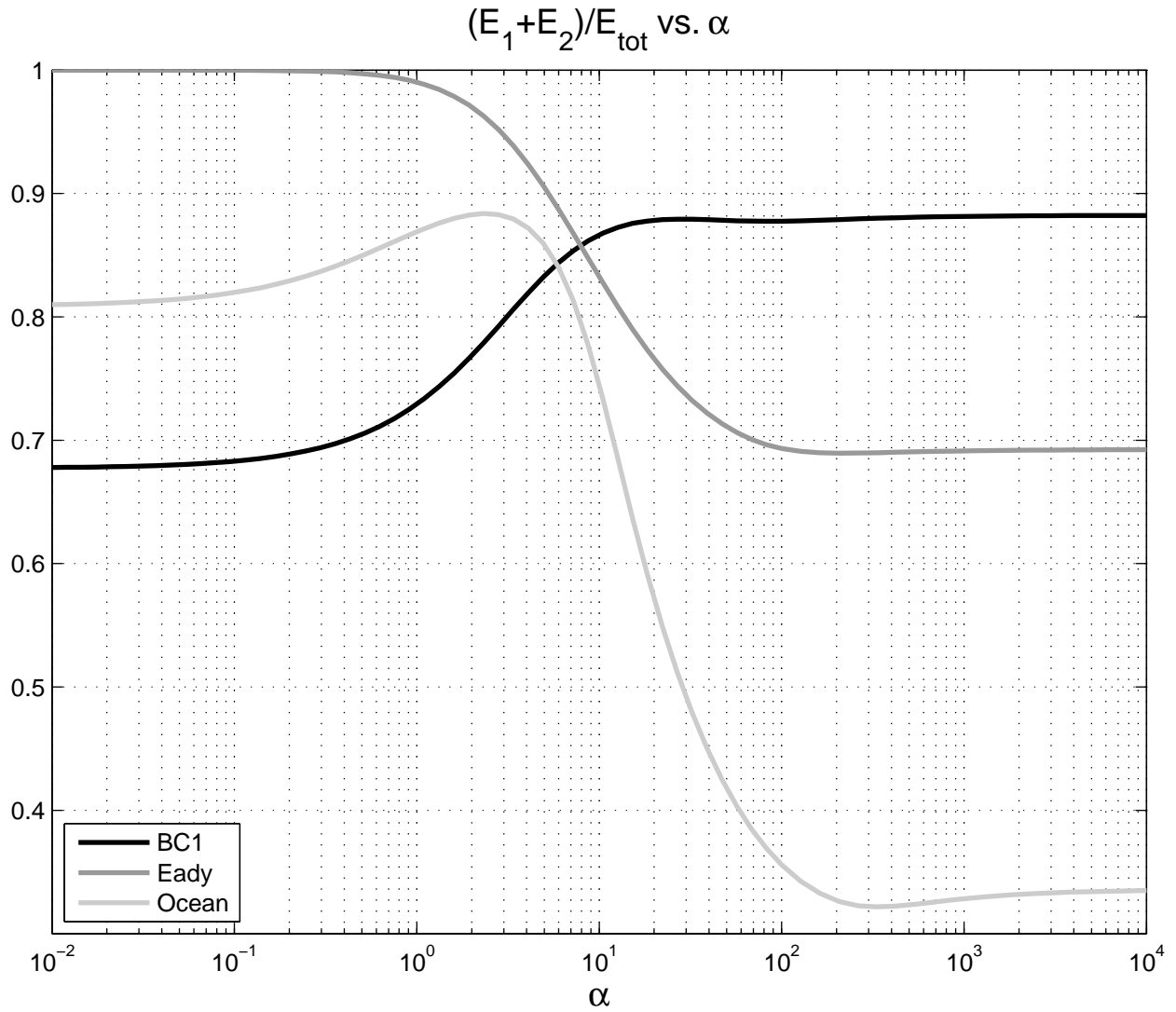
FIG. 5. Ratio of the energy content of the first two modes to the total energy as a function of $\alpha = \alpha_+ = \alpha_-$ for the BC1 and Eady simulations, and as a function of $\alpha = \alpha^+$ (with $\alpha_- \to \infty$) for the Ocean simulation.
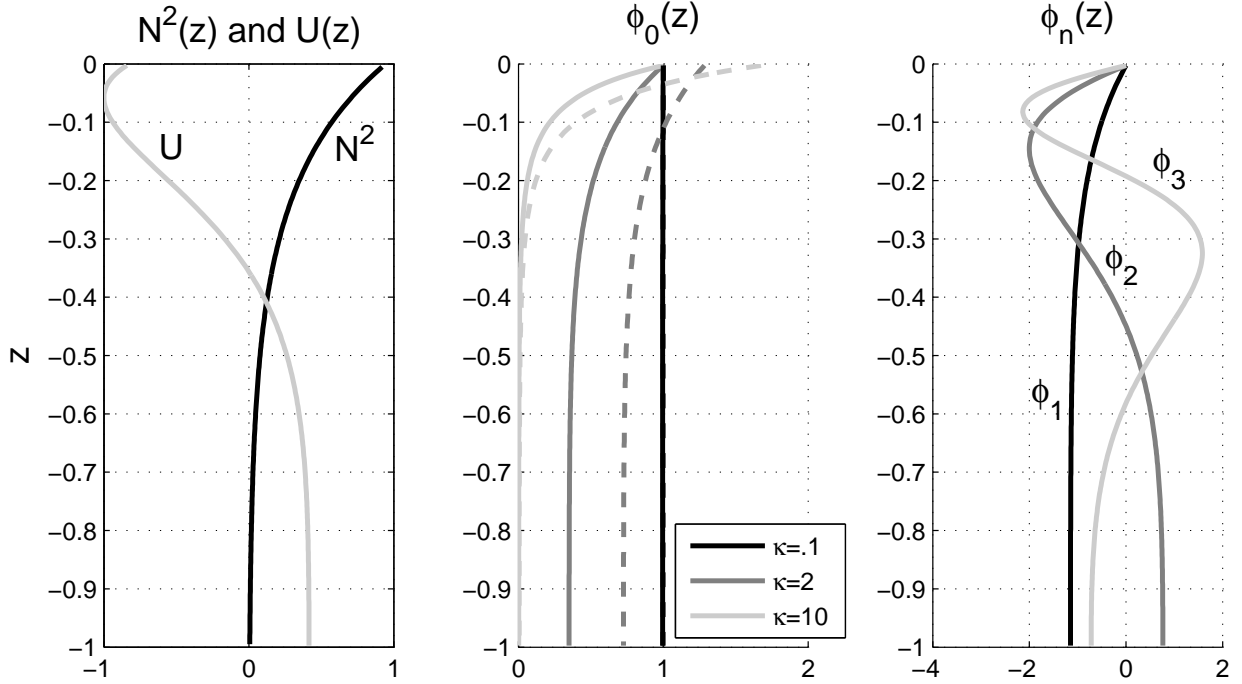
FIG. 6. Left: $N^2(z)$ and $U(z)$ for the Ocean simulation. Middle: the surface mode $\phi_0(z)$ with $\alpha_- \to \infty$ and $\alpha_+ \ll 1$ (solid) and $\alpha_+ = 2$ (dashed), for a range of wavenumbers κ (see legend). The $\kappa = .1$ lines are on top of each other. Right: The first three interior modes with $\alpha_+ \ll 1$ and $\alpha_- \to \infty$.
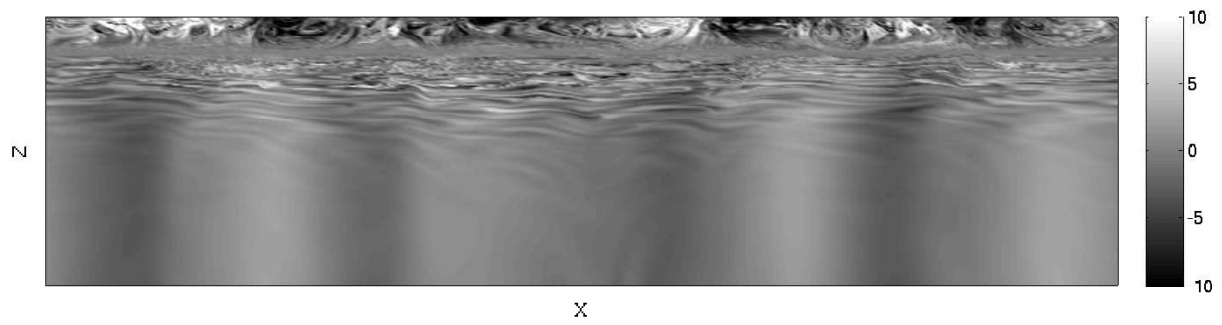
FIG. 7. Vertical slice of PV snapshot from the Ocean simulation. The flow has a complicated structure in the upper ocean, masking a more uniform flow at depth.
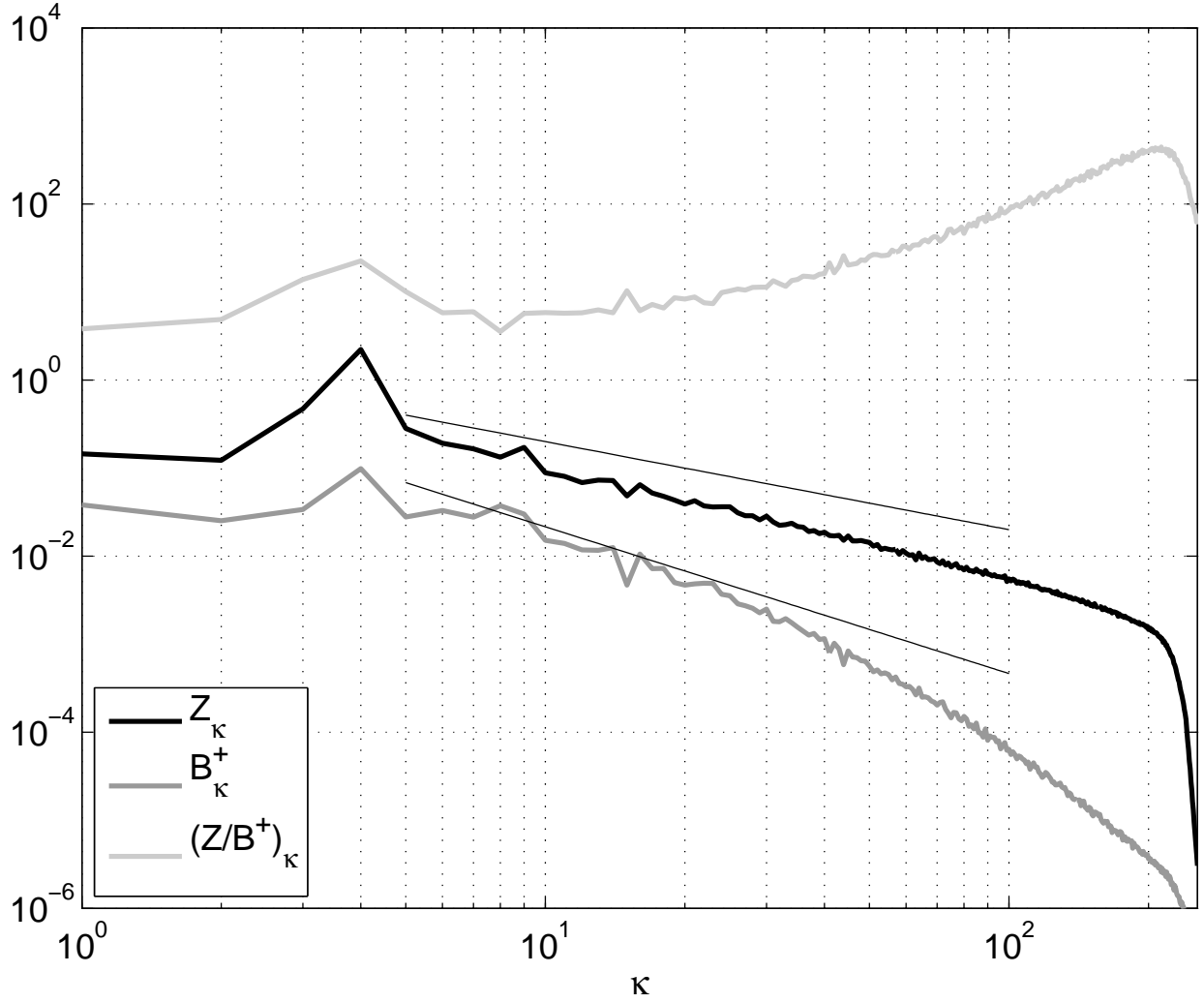
FIG. 8. Enstrophy Z_κ and surface buoyancy variance B_κ^+ as functions of wavenumber κ for the Ocean simulation (lines with slopes -1 and -5/3 are included for reference). The ratio Z_κ/B_κ^+, also shown, can be used to guide the choice of the weight α_+ for an effective projection basis.